Fast and accurate global multiphase arrival tracking: the irregular shortest-path method in a 3-D spherical earth model

Guo-Jiao Huang,[1] Chao-Ying Bai[1,2] and Stewart Greenhalgh[3]

[1]*Department of Geophysics, College of Geology Engineering and Geomatics, Chang'an University, Xi'an* 710054, *China. E-mail: chaoying_bai@yahoo.com*
[2]*Institute of Computing Geophysics, Chang'an University, Xi'an* 710054, *China*
[3]*Institute of Geophysics, ETH Zürich, CH* 8092, *Switzerland*

SUMMARY

The traditional grid/cell-based wavefront expansion algorithms, such as the shortest path algorithm, can only find the first arrivals or multiply reflected (or mode converted) waves transmitted from subsurface interfaces, but cannot calculate the other later reflections/conversions having a minimax time path. In order to overcome the above limitations, we introduce the concept of a stationary minimax time path of Fermat's Principle into the multistage irregular shortest path method. Here we extend it from Cartesian coordinates for a flat earth model to global ray tracing of multiple phases in a 3-D complex spherical earth model. The ray tracing results for 49 different kinds of crustal, mantle and core phases show that the maximum absolute traveltime error is less than 0.12 s and the average absolute traveltime error is within 0.09 s when compared with the AK135 theoretical traveltime tables for a 1-D reference model. Numerical tests in terms of computational accuracy and CPU time consumption indicate that the new scheme is an accurate, efficient and a practical way to perform 3-D multiphase arrival tracking in regional or global traveltime tomography.

Key words: Seismic tomography; Computational seismology; Wave propagation.

1 INTRODUCTION

Since the ground-breaking work of Aki & Lee (1976), in which medical computer-aided tomography (MCT) was introduced to seismology, seismic tomography has become a popular and effective way to image the inner structure and heterogeneity of the Earth (e.g. Anderson & Dziewonski 1982; Thomsen 1986; Pratt & Chapman 1992). Many 3-D earth models have been produced that have greatly advanced our knowledge about the complex structure, constitution and dynamics of the Earth's interior (e.g. PREM model, Dziewonski & Anderson 1981; IASP91 model, Kennett & Engdahl 1991; AK135 model, Kennett *et al.* 1995). However, continuing efforts should also be required to improve the theoretical aspects of seismic tomography as well as its applications, especially for real 3-D tomographic studies at the global or regional scales.

At the regional scale there exist several 3-D ray tracing algorithms for tomographic imaging (i.e. Steck *et al.* 1998; Keyser *et al.* 2002). But most global traveltime tomographic procedures still use a simple ray tracing method through a 1-D reference velocity model to accelerate the forward modelling process, because usually millions of multiphase traveltime data are involved. That is, ray paths are only calculated for a 1-D velocity model where velocity changes with depth or (radius) alone (e.g. the IASP91 model, Kennett & Engdahl 1991 or the AK135 model, Kennett *et al.* 1995), and the ray paths are fixed during the inversion process; ray path variations due to the lateral velocity heterogeneities being sought are not

considered (e.g. Su *et al.* 1994; van der Hilst *et al.* 1997). For small velocity variations about the reference model, such a linear inversion approach might at first seem acceptable, but in general a more rigorous procedure is required.

Bijwaard & Spakman (1999) examined ray path variations of first arriving *P* waves in 1-D and 3-D mantle velocity models, whereas Zhao & Lei (2004) checked pP, PP and PcP phases in 1-D and 3-D regional velocity models. Both studies found that there exists traveltime discrepancies larger than a few seconds and ray path deviations of nearly 100 km when converting from the 1-D to the 3-D velocity model. Therefore, investigation of the problem is important not only from a theoretical seismology point of view but also for practical imaging of the Earth's heterogeneous structure.

With the remarkable advances in computer technology over recent years and also the need to take into account lateral velocity heterogeneity, 3-D ray tracing methods in spherical coordinates based on real 3-D complex models have become feasible in regional and global traveltime tomographic studies. A few researchers have developed 3-D ray tracing schemes in spherical coordinates. For example, Bijwaard & Spakman (2000) exploited perturbation theory to develop a fast kinematic ray tracing algorithm to trace the first and later arrivals for some global seismic phases. Dahlen *et al.* (2000) used a combination of dynamic and kinematic ray tracing method to calculate the finite-frequency traveltimes and the corresponding Fréchet kernels. Zhao (2001) extended their original pseudo-bending ray tracing scheme (Zhao

et al. 1992) to the global scale to calculate the global later seismic arrivals.

The above 3-D ray tracing schemes are all based on two-point ray tracing, which means that one must repeat the ray tracing process when the receiver location is changed. This costs significant CPU time if on the order of a million rays for different phases are required in the tomographic reconstruction. Moreover, for the bending or pseudo-bending method, there exists a local minimum problem, while for the dynamic ray tracing method or the perturbation theory method, the difficulty of finding a source–receiver path increases with increasing complexity of the velocity model.

Grid/cell-based wavefront propagation methods, such as the finite difference eikonal equation solver (2-D/3-D, Vidale 1988, 1990, and revisions thereafter) and the shortest-path method (2-D, Moser 1991; 3-D, Klimeš & Kvasnička 1994; and modifications thereafter), are advantageous over the traditional two-point ray tracing schemes in that (1) they are capable of computing the traveltimes and related ray paths at all nodal points within the velocity model using the outward expanding wavefront technology, and are even able to locate ray paths in shadow zones; (2) they guarantee that a numerically stable global solution will be found; (3) they are very efficient computationally for common source point gathers compared with the two-point ray tracing method; (4) they are able to find first arrivals within continuous media, whereas for traditional ray tracing algorithms there is usually no guarantee that the selected arrival is a first or later arrival and (5) it is possible to trace multiple (transmitted, reflected and converted) arrivals when combined with a multistage scheme in the computations, for example, the multistage fast marching method (multistage FMM, Rawlinson & Sambridge 2004a,b), the multistage modified shortest-path method (multistage MSPM, Bai *et al.* 2009) and the multistage irregular shortest-path method (multistage ISPM, Bai *et al.* 2010).

De Kool *et al.* (2006) extended the above multistage FMM to 3-D spherical coordinates to track global later arrivals and concluded that it is an efficient and accurate 3-D ray tracing scheme. The previous studies (Bai *et al.* 2009, 2010) showed that in 2-D Cartesian coordinates for rectangular models both the multistage MSPM and ISPM are advantageous over the multistage FMM in the sense of computational accuracy and CPU time. They are expected to show similarly good performance in spherical coordinates for 3-D models. For this purpose we extend in this paper the multistage ISPM scheme to 3-D spherical coordinates to calculate 49 global multiple later arrival phases. We compare the computational accuracy against the AK135 global theoretical traveltime tables (Kennett *et al.* 1995) and also assess its computational efficiency.

2 MULTISTAGE ISPM IN SPHERICAL COORDINATES

Before introducing the multistage ISPM, we must first describe how the velocity model is parametrized in spherical coordinates.
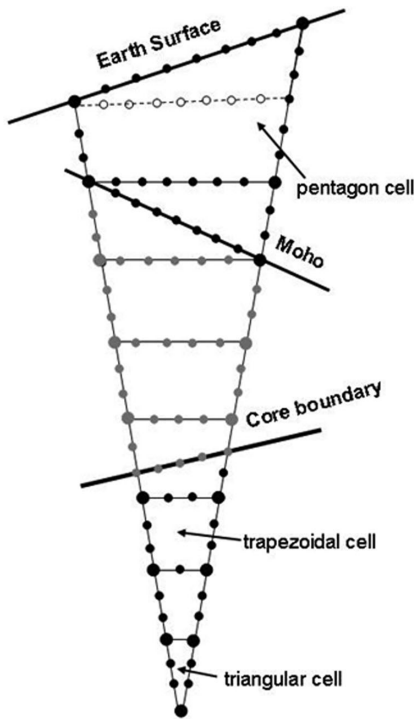
2.1 Earth model parametrization

Basically we can utilize irregular cells near an interface or velocity discontinuity, and use regular cells elsewhere. In the model parametrization, we first divide the subsurface model into several layers according to the interface lines (2-D) or surfaces (3-D) and parametrize each layer with regular or irregular cells. Secondary nodes are then uniformly distributed along the cell boundary (2-D
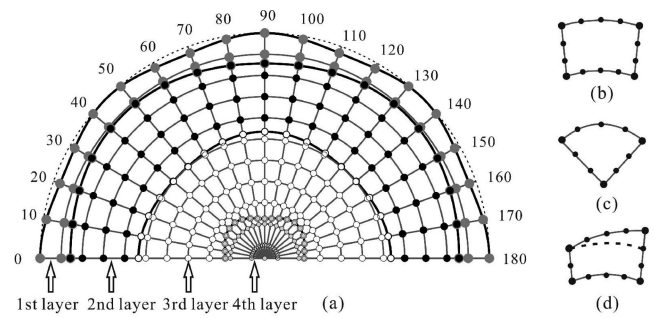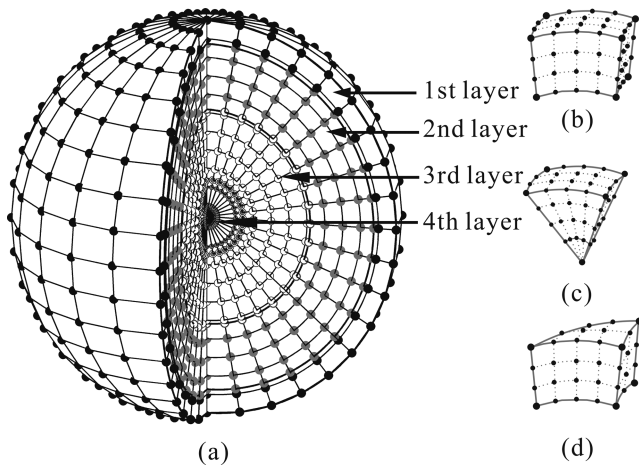

Figure 1. Model parametrization in 2-D spherical (polar) coordinates (diagram a, for clear representation, the secondary nodes are not depicted) and three kinds of cells used to divide the spherical model with undulated topography or discontinuities (diagrams b, c and d, in the figure the larger circles are the primary nodes and the smaller circles are the secondary nodes, respectively). In figure the different colour regions indicate different layers (from outer to inner is crust, mantle, outer core and inner core, respectively).

case) or cell surface (3-D case) so that each node (both primary and secondary) belongs to the specific (regular or irregular) cells. For example, in 2-D polar coordinates (see Fig. 1a), several cell types are available, for example, the triangular or the trapezoidal or pentagon cell. Here for reasons of simplicity we use an irregular cell (Figs 1c and d) near the irregular interfaces and a trapezoidal cell (Fig. 1b) elsewhere. We refer to the corner nodes of the trapezoidal or triangular or pentagon cell as the primary nodes. In order to improve the computational accuracy (ray coverage), we insert secondary nodes along the edges of the trapezoidal or triangular or pentagon cell. Furthermore, the pentagon cell can be divided into two cells; one is a trapezoidal cell and the other is a triangular cell (see Fig. 1d). Therefore, the basic cell type for the model parametrization is either a trapezoidal or triangular cell. The reader is referred to Bai *et al.* (2007) for primary and secondary node definitions, as well as for details on the modified shortest path method. The secondary node spacing can be simply uniform (or irregular), and determined by the metric distance. Fig. 2 shows part (fan-shaped) of a model parametrization, in which the cell length along the radial direction is the same, but its length in the zonal direction increases from the centre of the Earth outwards towards the free surface. Note that the secondary node spacing is the same for both directions.

In 3-D spherical coordinates we extend the above 2-D model parametrization to the 3-D case (see Fig. 3a). Note that other cells are also available, for example, polyhedron or tetrahedron (see, Ballard *et al.* 2009; Bai *et al.* 2012b). We use a trapezoidal prism (Fig. 3b) to divide the 3-D spherical earth model, except for the global and other irregular subsurface interfaces, where a trapezoidal cone or a hexahedral cell is used (Figs 3c and d). By similar considerations, the secondary nodes are inserted along the sides of the trapezoidal prism or trapezoidal cone or hexahedral cell. Inside each cell there are no nodes at all but sources and receivers may be located there. Note that for uniform model parametrization (that is, using regular trapezoidal prisms) it is possible not to record each node position, but for irregular cells it is necessary to record each node position, which accounts for the memory requirement. The total number of the nodes can be estimated by eq. (6) in Bai *et al.* (2007), but is at least 50 per cent less than that using such an equation because the added number of secondary nodes in the directions of longitude and latitude reduce from the Earth's surface to its centre (see Fig. 2) to maintain an equal secondary node spacing.

Figure 2. A small (or fan-shaped) section of model parametrization. In figure the larger circles are primary nodes and the smaller circles are the secondary nodes. The cell length (between the larger circles) along the radial direction is the same, but decreases from the Earth surface to the globe along the zonal direction. Note that the secondary node spacing (between the smaller circles) is the same for both directions. Note that the pentagon cell can be further divided into two cells, one is the trapezoidal and the other is the triangular cell (see the dashed line).

Figure 3. Model parametrization in 3-D spherical coordinates (diagram a, for clear representation, the secondary nodes are not depicted) and three kinds of cells used to divide the spherical model (diagrams b, c and d, in the figure the larger circles are primary nodes and the smaller circles are the secondary nodes, respectively).

2.2 Velocity interpolation function

In general, in both 2-D and 3-D spherical coordinates the velocity field is sampled at the primary nodes of the cell and a specified velocity function is defined across the cell, which links the primary and secondary nodes (including the source and receiver positions in
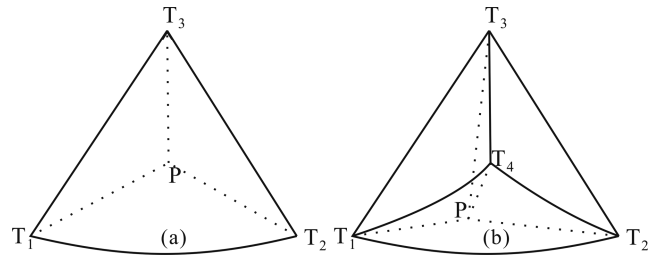
Figure 4. Diagrammatic explanation for interpolating velocity values.

a cell). For a 2-D trapezoidal cell, a bilinear Lagrangian interpolation function is used:

$$V(\mathbf{x}) = \sum_{k=1}^{4} \left[\prod_{\substack{l=1 \\ l \neq k}}^{4} \frac{(\mathbf{x} - \mathbf{x}_k^e)}{(\mathbf{x}_l^e - \mathbf{x}_k^e)} \right] \cdot V(\mathbf{x}_k^e), \tag{1}$$

where x_k^e and $V(x_k^e)$ ($k = 1, 2, \ldots, 4$) are the vector co-ordinates and the sampled velocity values at the primary nodes of the cell, respectively.

For a 3-D trapezoidal prism cell, a tri-linear Lagrangian interpolation function is used:

$$V(\mathbf{x}) = \sum_{k=1}^{8} \left[\prod_{\substack{l=1 \\ l \neq k}}^{8} \frac{(\mathbf{x} - \mathbf{x}_k^e)}{(\mathbf{x}_l^e - \mathbf{x}_k^e)} \right] \cdot V(\mathbf{x}_k^e), \tag{2}$$

where x_k^e and $V(x_k^e)$ ($k = 1, 2, \ldots, 8$) are the vector co-ordinates and the sampled velocity values at the primary nodes of the cell, respectively. For other special cells (2-D, Fig. 1c; 3-D, Figs 3c and d), the velocity values at the secondary node positions are determined by a triangular area interpolation function. For example, in triangular cells (2-D case) the following velocity interpolation function is used to determine the velocity values at the secondary node positions:

$$V(x_i) = \sum_{j=1}^{k} u_j v_j, \tag{3}$$

where v_j is the velocity value of the primary node at that triangular cell which includes the ith node and u_j is the area coordinates for that triangular cell. In the 2-D case $k = 3$, that is $u_1 = \frac{[PT_2T_3]}{[T_1T_2T_3]}$, $u_2 = \frac{[PT_1T_3]}{[T_1T_2T_3]}$, $u_3 = \frac{[PT_1T_2]}{[T_1T_2T_3]}$, where $[PT_1T_3]$, $[T_1T_2T_3]$ are respective areas of the triangles indicated in Fig. 4(a). In the 3-D case, $k = 4$, for example, $u_1 = \frac{[PT_2T_3T_4]}{[T_1T_2T_3T_4]}$, where $[PT_2T_3T_4]$ and $[T_1T_2T_3T_4]$ are the volume coordinates of the tetrahedrons $PT_2T_3T_4$ and $T_1T_2T_3T_4$ indicated in Fig. 4(b). In similar fashion we can easily obtain u_2, u_3 and u_4 (for details, refer to Bai *et al.* 2011, 2012a). Note that the subsurface interface is defined by two different velocity values at all points along its extent [i.e. sampled values just above (upper values) and just below (lower values) the interface]. As with the AK135 model, the velocity interpolation follows a similar rule such that for reflections from the interface we use the upper velocity values, and for critical refraction just below the interface or transmission into the lower layer, we use the lower velocity values.

2.3 Irregular shortest-path ray tracing scheme

Basically, the irregular shortest-path method (ISPM, Bai *et al.* 2010) for ray tracing is more complicated than the modified shortest-path method (MSPM, Bai *et al.* 2009), because the wave propagation is no longer along the expanding regular square (or circle in spherical coordinates) wavefront, but along the expanding irregular one.

Therefore, the technical treatment of the ISPM for wavefront propagation is quite different from that used in the MSPM, where only the cell length is used to expand the square (or circular) wavefront propagation. In order to expand the wavefront propagation, we can exploit a similar approach used in the MSPM ray tracing, but use the metric distance criterion (not the cell length) to control the wavefront propagation (for details, see Bai *et al.* 2010, 2011, 2012a). Alternatively, in the model parametrization, the neighbouring cells around each cell can be indexed; therefore it is easy to conduct wavefront propagation throughout the whole model. In addition, with the introduction of second level forward star scheme, the total number of nodes can be sufficiently reduced and therefore less computer memory is required. In this fashion, the computing accuracy with the second level forward star scheme can be largely improved (say, two to three times in general) over the accuracy possible with the first level forward star scheme applied in the multistage ISPM scheme (see, Bai *et al.* 2011).

In calculating the minimum traveltimes and locating the associated ray paths for all grid nodes, we can gradually expand outwards from the source the volume of the computed nodes (simply belong to all neighbouring cells or determined by the metric distance criterion) by continually adding the undetermined neighbouring nodes of the cells to the computed nodes. The wavefront expansion is realized cell by cell. The connection between the nodes is restricted within each cell. It is referred to as the first level forward star scheme. In the second level forward star scheme, the node connections are not only within current cell, but also with neighbouring cells (see Bai *et al.* 2011). In this process one should start with the node that has a minimum traveltime in the subset N_j (where N_j is the total number of computed nodes in the current wavefront) so as to keep track of the first arrival times for the undetermined nodes. An interval sorting method (Klimeš & Kvasnička 1994) is used so that the larger traveltimes are deleted; only the minimum traveltime and the related ray path are retained. The minimum traveltime from a source node i to an undetermined node j in a cell can be expressed as

$$t_{i \cdot j} = \min_{i \in N_j} \left\{ t_i + \frac{2D(\mathbf{x}_i, \mathbf{x}_j)}{[V(\mathbf{x}_i) + V(\mathbf{x}_j)]} \right\}, \tag{4}$$

where $D(x_i, x_j)$ is the distance between the source node i and the undetermined node j, and $V(x_i)$ and $V(x_j)$ are the velocity values
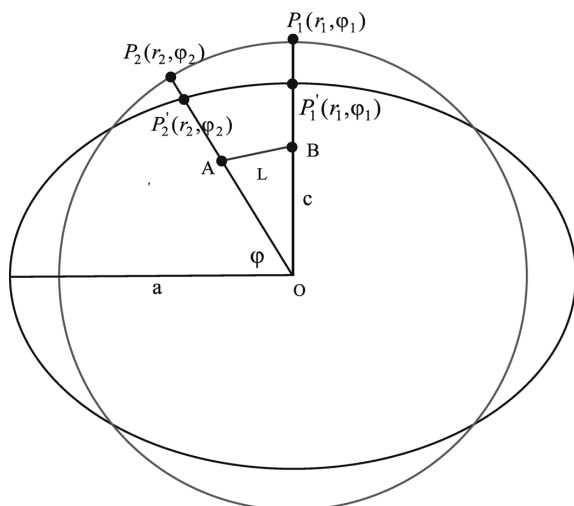
at the ith and the jth node positions. If the ith or the jth nodes do not belong to the subset of primary nodes, then the velocity value at such a node position in a cell can be obtained from the above Lagrangian or B-spline interpolation function, dependent on which
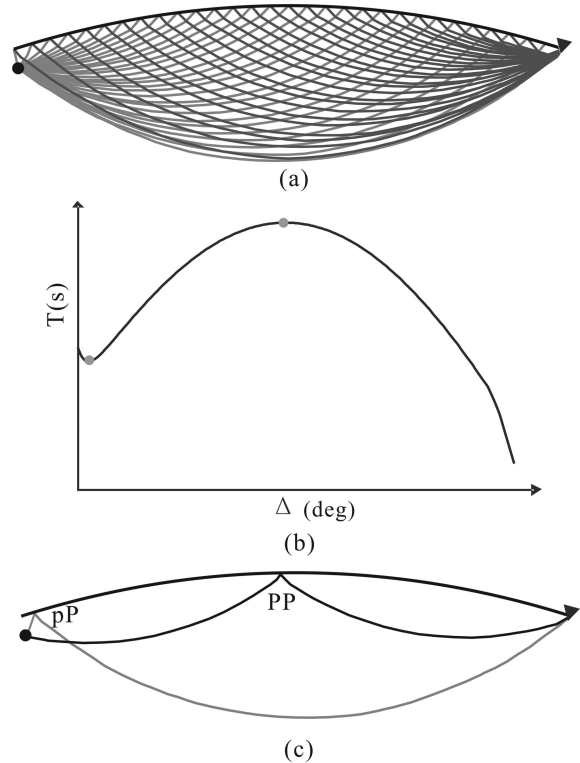

Figure 6. Diagrammatic calculation of later arrivals following the minimax time path (diagram a: the ray paths from both the source and receiver to the sampled interface; diagram b: summed time curve on the sampled interface, showing two extreme locations, and diagram c: the ray paths for pP and PP according to Fermat's Principle of stationary minimax time path.

Figure 5. Diagram showing correction for Earth ellipticity. The radius varies over the surface of the ellipsoid.
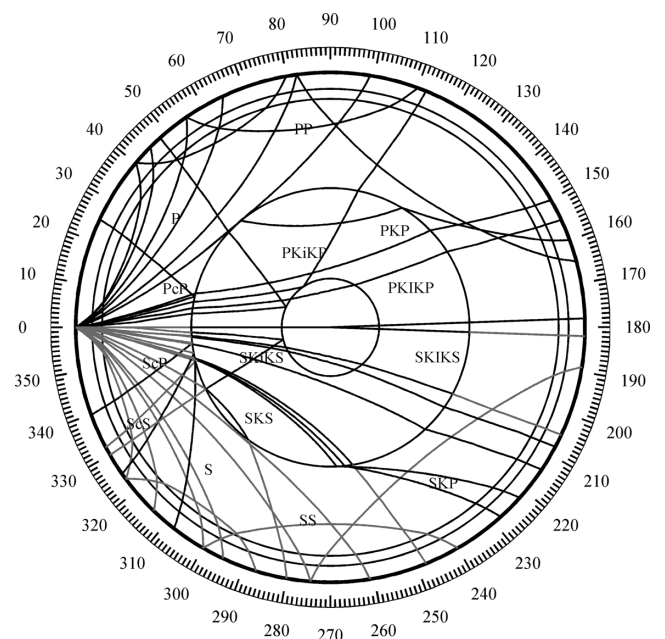

Figure 7. Ray paths of some global phases calculated by using the multistage ISPM scheme (in the figure black lines are for *P*-mode phases and grey lines for *S*-mode phases).

cell the node belongs to, a regular or an irregular cell. Furthermore, in this process the order number of the incident point (node) i^* giving the minimum traveltime to the node j is recorded for the co-ordinates of the related ray path.

2.4 Multistage scheme of computation

According to the layered spherical earth model (Fig. 1a or Fig. 3a), we can divide the earth model into several spherical layers (or shells) corresponding to the major velocity discontinuities. For illustrative purposes consider as an example the Moho discontinuity which separates the crust and mantle. A simulated downwind wavefront (P_1 phase) is propagated through the crust (or upper computational domain) until it impinges on all sampled nodes of the Moho subsurface interface (In our notation convention: P or S represents a compressional or shear wave, respectively, and the subscript or superscript indicates a downwind or upwind seismic wave propagating in different regions, respectively). At this stage the independent computational domain is halted at the upper computational domain and we are left with a narrow band of traveltime values

defined along the sampled (Moho) subsurface interface. From here, a downwind propagation of a transmitted wave (P_1P_2) or transmitted and mode-converted branch (P_1S_2 phase) can be simulated by re-initializing it, starting at the sampled node position of the (Moho) interface with the minimum traveltime (i.e. according to Huygens Principle, the node is treated as one new source point in the wavefront). The wave is then projected into the adjacent mantle (or lower) layer. Meanwhile, an upwind-propagating wavefront consisting of a reflected branch (P_1P^1 or PmP phase) or a reflected and converted branch (P_1S^1 or PmS phase) can now be obtained by re-initializing the wavefront and starting at the sampled node position with the minimum traveltime, from the narrow band of the Moho interface into the incident layer (or crust). Different velocity models (i.e. P or S) are used if wave-mode conversion occurs at the subsurface interfaces. In summary, the multiple arrivals are the different combinations or conjugations, via velocity discontinuities (i.e. subsurface interfaces), of the incident, reflected and converted phases, which obey Snell's Law, Fermat's Principle and Huygens Principle. In order to trace complex ray paths that may refract, reflect and/or convert at the velocity discontinuities, we use the so-called 'phase code' in the input file to control how the ray path progresses
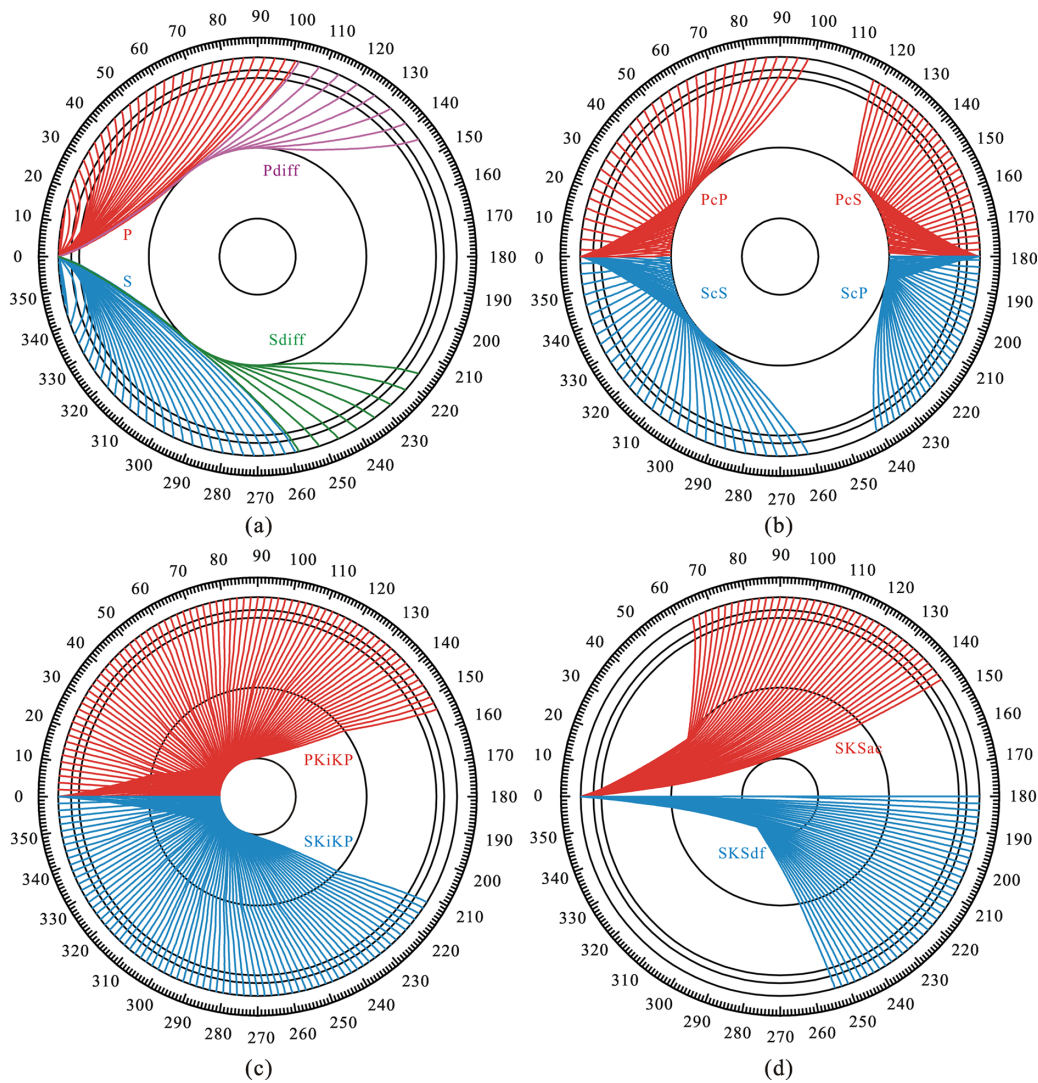
Figure 8. Ray paths for direct arrivals (P and S), diffracted arrivals from the mantle-core boundary (Pdiff and Sdiff), reflected arrivals from the mantle–core boundary (PcP, PcS, ScS and ScP), reflected arrivals from the outer core-inner core boundary (PKiKP and SKiKP), and arrivals crossing the outer core (SKSac) and inner core (SKSdf), by directly using the multistage ISPM scheme.
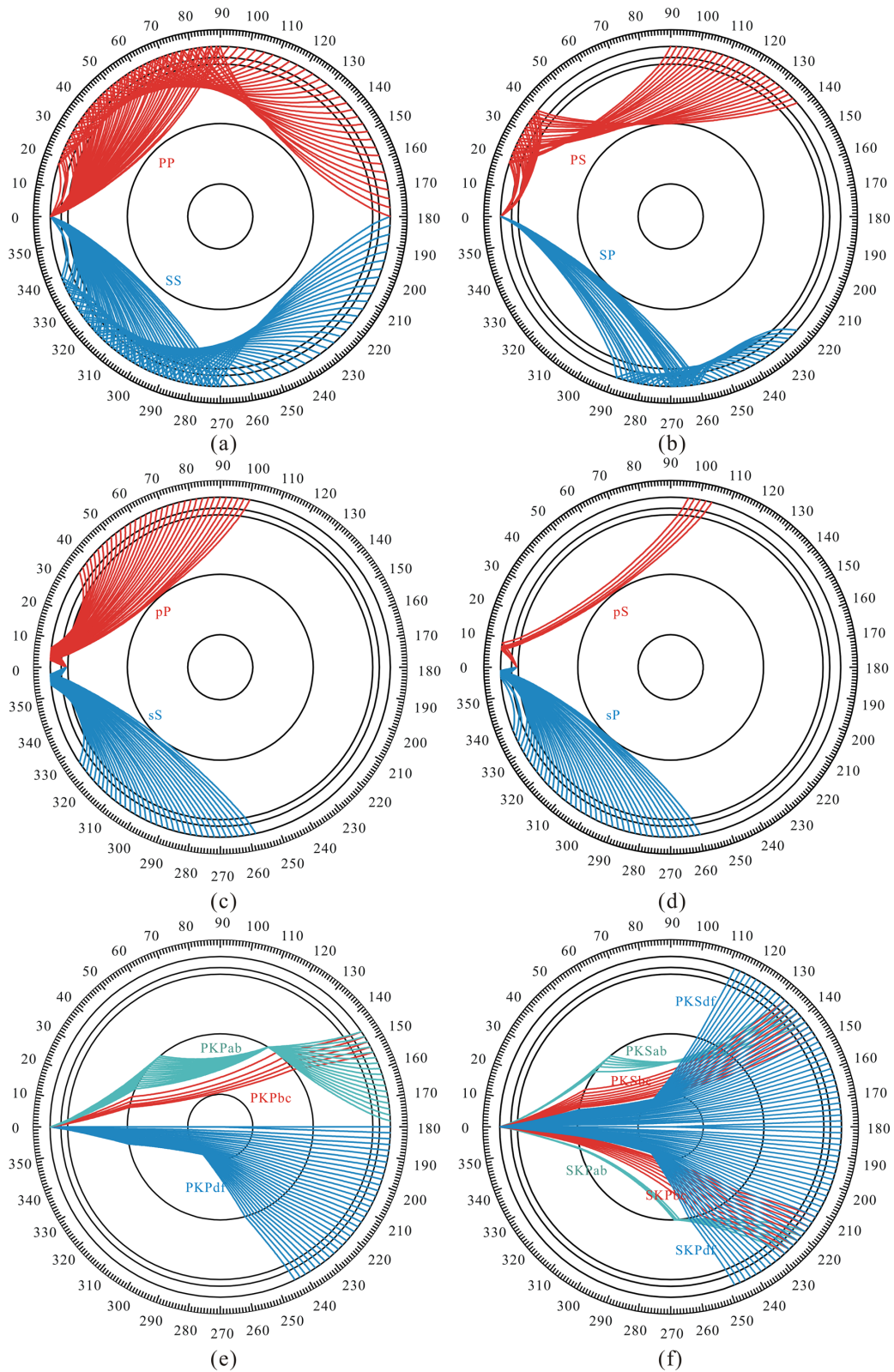
Figure 9. Ray paths computed by the multistage ISPM incorporated with an extreme solution of the summed traveltime curve for reflections from the Earth's free surface (diagram a: PP and SS), Earth's free surface reflected mode conversions (diagram b: PS and SP), deep reflections (diagram c: pP and sS) for a focal depth of 100.0 km, deep reflected mode conversions (diagram d: pS and sP) for a focal depth of 100.0 km, pure core phases (diagram e: PKPab, PKPbc and PKPdf) and mode-converted core phases (diagram f: PKSab, PKSbc, PKSdf, SKPab, SKPbc and SKPdf).
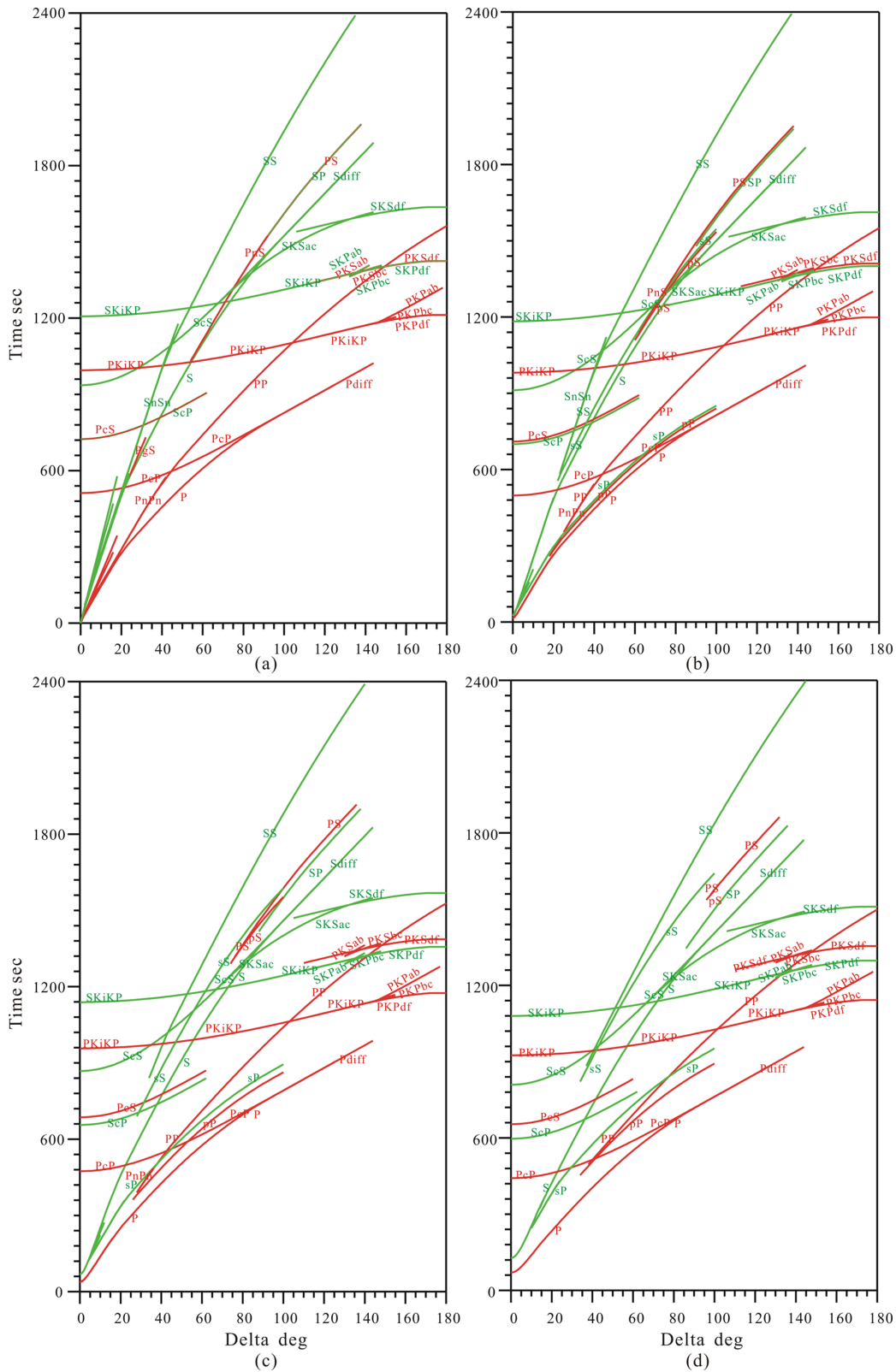
Figure 10. The time–distance curves calculated for the 49 global phases with different focal depths (diagram a: for focal depth of 0.0 km; diagram b: for focal depth of 100.0 km; diagram c: for focal depth of 300.0 km and diagram d: for focal depth of 600.0 km). In figure, the black lines (red online) indicate the *P*-mode phases and the grey lines (green online) the *S*-mode phases.

through the earth model volume. That is, whether the ray goes up or down from the source, which subsurface interface is crossed, and at which subsurface interface(s) the ray is refracted, reflected and/or converted.

2.5 Radius correction for Earth ellipticity

The Earth is not a perfect sphere but an ellipsoid (see Fig. 5 for 2-D case), so it is necessary to correct the Earth radius at different surface locations (Snoke & Lahr 2001). There are two ways to make ellipticity corrections: one is to do the correction after the traveltime calculation and the other is to directly calculate the traveltime on the ellipsoidal Earth. The ellipticity has a direct influence on the radius (Dziewonski & Gilbert 1976) and the ellipticity correction is then the sum of contributions due to lengthening or shortening of the ray at its ends. The actual radius r of an ellipsoidal Earth at latitude φ can be written as

$$r = a(1 - e\,\sin^2\varphi), \tag{5}$$

Table 1. The maximum (E1) and mean (E2) absolute time errors, and the maximum (E3) and mean (E4) relative time errors against the AK135 theoretical traveltime tables for a focal depth of 0.0 km.

Phases	E1 (s)	E2 (s)	E3 (per cent)	E4 (per cent)
P	0.07	0.01	0.01	0.00
S	0.08	0.05	0.01	0.00
PcP	0.05	0.01	0.01	0.00
PcS	0.04	0.01	0.01	0.00
ScS	0.08	0.05	0.01	0.00
ScP	0.04	0.01	0.01	0.00
PP	0.05	0.01	0.01	0.00
PS	0.06	0.02	0.00	0.00
SS	0.10	0.05	0.01	0.00
SP	0.06	0.02	0.00	0.00
Pdiff	0.05	0.04	0.01	0.00
Sdiff	0.08	0.06	0.01	0.00
SKiKP	0.09	0.05	0.01	0.00
PKiKP	0.07	0.03	0.01	0.00
Pb	0.03	0.02	0.05	0.03
Sb	0.03	0.02	0.03	0.02
Pn	0.02	0.01	0.03	0.01
Sn	0.06	0.05	0.07	0.02
Pg	0.00	0.00	0.00	0.00
Sg	0.06	0.02	0.03	0.01
PbPb	0.05	0.05	0.10	0.04
SbSb	0.05	0.04	0.04	0.02
PgPg	0.01	0.00	0.01	0.00
SgSg	0.06	0.01	0.03	0.00
PnPn	0.05	0.03	0.05	0.01
SnSn	0.08	0.06	0.07	0.02
PgS	0.04	0.02	0.01	0.00
PnS	0.09	0.07	0.01	0.01
PKPab	0.11	0.06	0.01	0.00
PKPbc	0.02	0.01	0.00	0.00
PKPdf	0.07	0.02	0.01	0.00
PKSab	0.02	0.02	0.00	0.00
PKSbc	0.02	0.01	0.00	0.00
PKSdf	0.09	0.02	0.01	0.00
SKPab	0.02	0.02	0.00	0.00
SKPbc	0.02	0.01	0.00	0.00
SKPdf	0.09	0.02	0.01	0.00
SKSac	0.06	0.03	0.00	0.00
SKSdf	0.10	0.02	0.01	0.00

Table 2. Same as for Table 1, but with a focal depth of 100.0 km.

Phases	E1 (s)	E2 (s)	E3 (per cent)	E4 (per cent)
P	0.03	0.01	0.02	0.00
S	0.08	0.04	0.02	0.00
PcP	0.04	0.01	0.01	0.00
PcS	0.03	0.01	0.00	0.00
ScS	0.08	0.04	0.01	0.00
ScP	0.04	0.01	0.01	0.00
PP	0.05	0.01	0.01	0.00
PS	0.07	0.02	0.00	0.00
SS	0.10	0.06	0.01	0.00
SP	0.01	0.01	0.00	0.00
Pdiff	0.04	0.04	0.00	0.00
Sdiff	0.05	0.04	0.00	0.00
SKiKP	0.07	0.04	0.01	0.00
PKiKP	0.07	0.02	0.01	0.00
Pn	0.02	0.01	0.02	0.01
Sn	0.05	0.03	0.03	0.01
PnPn	0.04	0.01	0.01	0.00
SnSn	0.07	0.06	0.01	0.01
PnS	0.10	0.07	0.01	0.01
pP	0.02	0.01	0.00	0.00
pS	0.06	0.04	0.00	0.00
sS	0.06	0.03	0.01	0.00
sP	0.02	0.01	0.01	0.00
pPn	0.02	0.01	0.01	0.00
sPn	0.04	0.02	0.04	0.02
sPg	0.05	0.05	0.04	0.03
sPb	0.04	0.04	0.07	0.04
PKPab	0.10	0.06	0.01	0.00
PKPbc	0.02	0.01	0.00	0.00
PKPdf	0.07	0.02	0.01	0.00
PKSab	0.01	0.01	0.00	0.00
PKSbc	0.02	0.01	0.00	0.00
PKSdf	0.10	0.02	0.01	0.00
SKPab	0.02	0.02	0.00	0.00
SKPbc	0.02	0.01	0.00	0.00
SKPdf	0.09	0.02	0.01	0.00
SKSac	0.04	0.02	0.00	0.00
SKSdf	0.10	0.02	0.01	0.00

where a is the semi-major (long) axis of the ellipsoid, and e is the eccentricity. The distance (L) between any pair of node locations within a cell (for triangle OAB) can be calculated as follows:

$$L = \sqrt{(r'_{p_A} - z_A)^2 + (r'_{p_B} - z_B)^2 - 2(r'_{p_A} - z_A)(r'_{p_B} - z_B)\cos(\varphi_2 - \varphi_1)}, \tag{6}$$

where z_A and z_B are the depths of two nodes (A and B), respectively, r'_{p_A} and r'_{p_B} are the respective radii at the crossing points A and B (see Fig. 5).

2.6 Fermat's principle of the minimax time path and extremal solutions

Note that the nomenclature specifying the seismic phases in the AK135 traveltime tables was modified to the standard nomenclature proposed by Storchak *et al.* (2003), so in the following discussion we make use of this symbolism. It is well known that the grid/cell based wavefront propagation schemes are only capable of tracking first arrivals (i.e. P, S, Pn, Sn, Pg, Sg, Pb and Sb) and some kinds

Table 3. Same as for Table 1, but with a focal depth of 300.0 km.

Phases	E1 (s)	E2 (s)	E3 (per cent)	E4 (per cent)
P	0.02	0.01	0.05	0.00
S	0.08	0.04	0.01	0.00
PcP	0.03	0.01	0.01	0.00
PcS	0.03	0.02	0.00	0.00
ScS	0.08	0.04	0.01	0.00
ScP	0.03	0.01	0.00	0.00
PP	0.06	0.01	0.01	0.00
PS	0.08	0.03	0.00	0.00
SS	0.11	0.06	0.01	0.00
SP	0.08	0.01	0.01	0.00
Pdiff	0.05	0.04	0.01	0.00
Sdiff	0.05	0.04	0.00	0.00
SKiKP	0.06	0.04	0.01	0.00
PKiKP	0.06	0.02	0.01	0.00
Pn	0.02	0.01	0.02	0.01
PnPn	0.05	0.01	0.01	0.00
PnS	0.10	0.09	0.01	0.01
pP	0.04	0.02	0.01	0.00
pS	0.05	0.04	0.00	0.00
sS	0.06	0.03	0.00	0.00
sP	0.02	0.01	0.01	0.00
pPn	0.01	0.01	0.00	0.00
sPn	0.04	0.03	0.03	0.01
sPg	0.07	0.07	0.04	0.03
sPb	0.05	0.05	0.03	0.03
PKPab	0.10	0.06	0.01	0.00
PKPbc	0.02	0.01	0.00	0.00
PKPdf	0.08	0.02	0.01	0.00
PKSab	0.01	0.00	0.00	0.00
PKSbc	0.03	0.02	0.00	0.00
PKSdf	0.11	0.03	0.01	0.00
SKPab	0.01	0.01	0.00	0.00
SKPbc	0.02	0.01	0.00	0.00
SKPdf	0.09	0.02	0.01	0.00
SKSac	0.04	0.02	0.00	0.00
SKSdf	0.10	0.02	0.01	0.00

Table 4. Same as for Table 1, but with a focal depth of 600.0 km.

Phases	E1 (s)	E2 (s)	E3 (per cent)	E4 (per cent)
P	0.02	0.01	0.03	0.00
S	0.08	0.04	0.01	0.00
PcP	0.03	0.01	0.01	0.00
PcS	0.03	0.02	0.00	0.00
ScS	0.08	0.04	0.01	0.00
ScP	0.03	0.01	0.01	0.00
PP	0.06	0.01	0.01	0.00
PS	0.08	0.03	0.00	0.00
SS	0.11	0.06	0.01	0.00
SP	0.07	0.01	0.01	0.00
Pdiff	0.04	0.04	0.01	0.00
Sdiff	0.05	0.04	0.00	0.00
SKiKP	0.06	0.04	0.01	0.00
PKiKP	0.06	0.02	0.01	0.00
pP	0.03	0.02	0.01	0.00
pS	0.05	0.04	0.00	0.00
sS	0.06	0.04	0.00	0.00
sP	0.03	0.01	0.01	0.00
sPn	0.04	0.03	0.01	0.01
sPb	0.08	0.08	0.02	0.02
PKPab	0.09	0.06	0.01	0.00
PKPbc	0.02	0.02	0.00	0.00
PKPdf	0.08	0.02	0.01	0.00
PKSab	0.01	0.00	0.00	0.00
PKSbc	0.03	0.02	0.00	0.00
PKSdf	0.12	0.03	0.01	0.00
SKPab	0.02	0.01	0.00	0.00
SKPbc	0.02	0.01	0.00	0.00
SKPdf	0.10	0.02	0.01	0.00
SKSac	0.04	0.02	0.00	0.00
SKSdf	0.11	0.02	0.01	0.00

of initial reflections, transmissions and mode conversions (i.e. PmP, SmS, PmS, SmP, PnPn, SnSn, PgPg, SgSg, PcP, ScS, PcS, ScP, etc.), which are the ray paths following the minimum traveltime, while, it is not possible to calculate other later arrivals which follow the stationary maximum or minimax ray paths (i.e. PKPab, pP, sS, PP, SS, sP, pS, etc.). Fermat's Principle states that the ray (or energy) will follow an extremal time path, that is, it takes that path l between two points, which takes an extreme traveltime t (i.e. the shortest (minimum) or the longest (maximum) possible traveltime, or a point of inflection with $\partial t/\partial l = 0$). Such a path is called stationary. In the case of a stationary time path the three possibilities identified above depend on the sign of the higher derivatives of $\partial t/\partial l$ (e.g. Cerveny 2001; Bormann *et al.* 2009):

(1) $\partial^2 t/\partial l^2 > 0$, the ray follows a true minimum traveltime path (i.e. P, S, Pn, Sn, Pg, Sg, Pb, Sb; PmP, SmS, PmS, SmP, PnPn, SnSn, PgPg, SgSg, PcP, ScS, PcS, ScP, etc.),
(2) $\partial^2 t/\partial l^2 < 0$, the ray follows a maximum traveltime path (i.e. PKPab) and
(3) $\partial^2 t/\partial l^2 = 0$, that is, in case of an inflection point of the traveltime curve, the ray follows a minimax traveltime path (i.e. pP, sS, PP, SS, sP, pS, etc.).

For example, pP and PP are the same kind of surface reflections from the Earth's free surface; the former follows the minimum time path and the latter follows the maximum time path. For those kinds of stationary minimax time ray paths we can use an extreme solution of the summed ray fields to calculate the related ray paths and the corresponding traveltimes, as illustrated in Fig. 6. The principle of the extreme solution of the summed ray fields is that we calculate ray paths and the related traveltimes from both the source and receiver to the sampled subsurface interface (Fig. 6a) and obtain the summed traveltime curve (2-D, see black curve at the Fig. 6b) or surface (3-D) and locate extreme locations (see grey dot on the curve of the Fig. 6b), which correspond to the reflection points. That is, the minimum extremum on the summed traveltime curve is the pP traveltime and the maximum is the PP reflection. Finally, we link the ray paths and sum the traveltimes from the source and receiver to the reflector, which constitute the real pP and PP traveltimes and the corresponding ray paths (Fig. 6c). Note that the summed traveltime curve (2-D) or surface (3-D) to locate the minima, maxima and saddle points are along the reflecting interface (2-D) or subsurface interface (3-D). The reader is referred to Bai *et al.* (2012b) for a detailed explanation.

3 THEORETICAL TRAVELTIMES OF GLOBAL SEISMIC PHASES

To validate the new ray tracing scheme in terms of computational accuracy and efficient performance, we now calculate the traveltimes and corresponding ray paths for 49 crustal, mantle and core phases and compare our results with the AK135 global theoretical
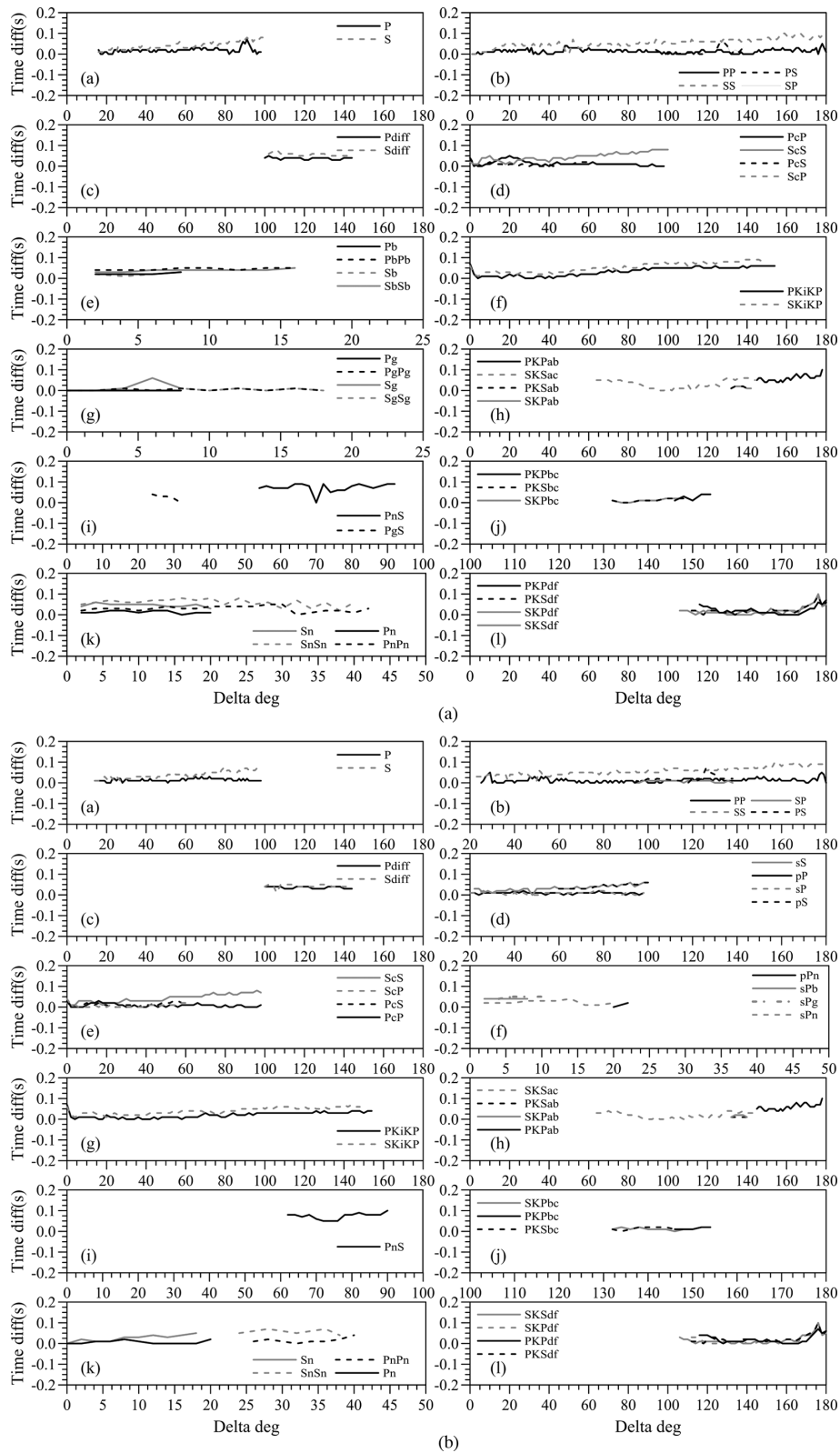
Figure 11. (a) The time difference (error) curves between the calculated and the AK 135 theoretical traveltime tables for a focal depth of 0.0 km (diagram a: for *P* and *S*; diagram b: for PP, SS, PS and SP; diagram c: for Pdiff and Sdiff; diagram d: PcP, ScS, PcS and ScP; diagram e: for Pb, Sb, PbPb and SbSb; diagram f: for PKiKP and SKiKP; diagram g: Pg, Sg, PgPg and SgSg; diagram h: for PKPab, SKSac, SKPab and PKSab; diagram i: for PgS and PnS; diagram j: for PKPbc, SKPbc and PKSbc; diagram k: for Pn, Sn, PnPn and SnSn and diagram l: for PKPdf, SKPdf, SKSdf and PKSdf). (b) Same as for Fig. 10 but for a focal depth of 100.0 km. (c) Same as Fig. 10(a) but for a focal depth of 300.0 km. (d) Same as Fig. 10(a) but for a focal depth of 600.0 km.
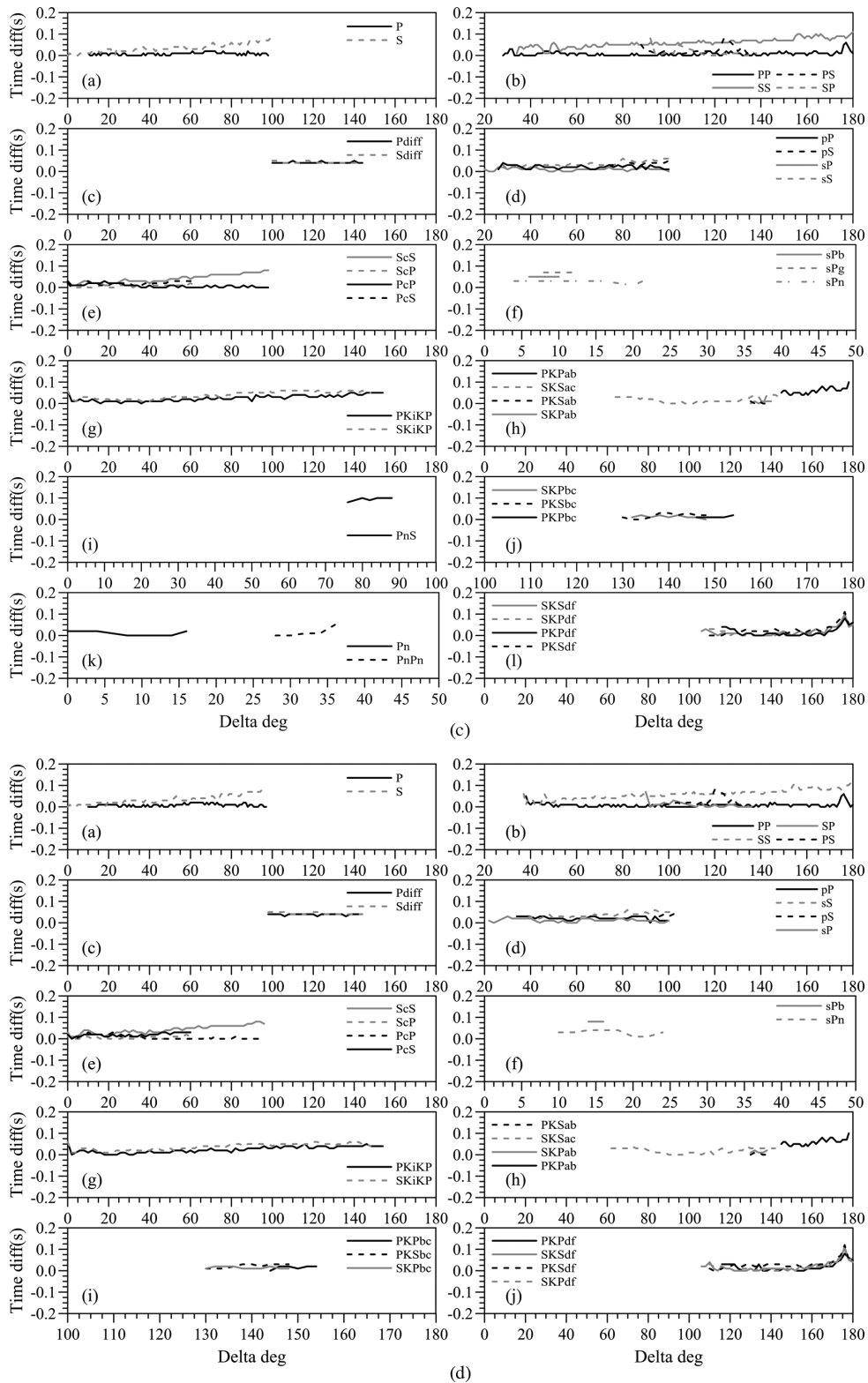
Figure 11. (*Continued.*)

traveltime tables (Kennett *et al.* 1995). The reference earth model in this case is a 1-D spherically layered model and there are eight velocity discontinuities located at depths of 20, 35, 210, 410, 660, 2740, 2891.5 and 5153.5 km, respectively (see AK135 model, Kennett *et al.* 1995). For the model parametrization, we use a cell size of $0.5° \times 20$ km depth to divide the spherical earth model (re-

fer to Fig. 1a), and a secondary node spacing of 1.0 km $\times 1.0$ km is applied. Fig. 7 shows some calculated ray paths including direct arrivals (*P* and *S*), Earth surface reflections (PP and SS), outer core reflections (PcP, ScS and ScP), inner core reflections (PKiKP and SKiKS) and core refracted phases (SKP, SKS and PKP).

According to the AK135 traveltime tables, the calculated 49 global phases include: (1) crustal phases: Pg, Pb, Pn, PgPg, PbPb, PnPn, PgS, PnS, Sg, Sb, Sn, SgSg, SbSb, SnSn; (2) mantle phases: P, S, PP, PS, SP, SS, PcP, PcS, ScS, ScP, Pdiff, Sdiff; (3) core phases: PKP (PKPab, PKPbc and PKPdf), PKS (PKSab, PKSbc and PKSdf), SKP (SKPab, SKPbc and SKPdf), SKS (SKSac and SKSdf), PKiKP, SKiKP and (4) depth phases: pP, pS, sS, sP, pPn, sPn, sPg, sPb. Fig. 8 shows ray trajectories of calculated global phases which obey the minimum time paths in which the *P* and *S* wave become diffracted waves (Pdiff and Sdiff) when they graze the core mantle boundary (or CMB) with increasing epicentral distance, due to the low *P*-wave velocity in the outer core (where *S* velocity is zero, see Fig. 8a). Because the *P*-wave velocity of the outer core is significantly lower than the *P*-wave velocity at the base of the mantle, but larger than the *S*-wave velocity at the base of the mantle, the incident angle of the phase PKiKP is reduced significantly when it leaves the mantle and enters the outer core. By the same argument, the outgoing angle of phase PKiKP is increased when it leaves the outer core and enters the mantle (see Fig. 8c).

Fig. 9 depicts the ray trajectories for the calculated global phases which follow the stationary minimax time paths. For the pairs of Earth free—surface reflections, the maximum extremal solution coincides with the phases (PP, PS, SP, SS, see Figs 9a and b), whereas the minimum extremal solution corresponds to the deep reflections and /or converted phases (pP, pS, sP and sS, see Figs 9c and d). When the rays cross the inner core the phenomenon of caustics occurs for the families of phases (PKPab, PKSab and SKPab) and (PKPbc, PKSbc and SKPbc). The former correspond to the maximum time paths and the latter coincide with the minimum time paths (see Figs 9e and f). Note that for the phases (PKPdf, PKSdf and SKPdf) it is possible to directly apply the multistage ISPM to calculate them.

4 COMPARISONS WITH THE AK135 TRAVELTIME TABLES

To make a detailed comparison with the AK135 traveltime tables, we use four different source focal depths (0.0, 100.0, 300.0 and 600.0 km) as listed in the AK135 traveltime tables. The time–distance curves of the calculated 49 different global phases for the different focal depths are shown in Fig. 10 (diagram a: for focal depth of 0.0 km; diagram b: for focal depth of 100.0 km; diagram c: for focal depth of 300.0 km and diagram d: for focal depth of 600.0 km). From Fig. 10 we see that for the same kind of global phases the time–distance curves have similar features, regardless of the focal depth, and the time–distance curves of the reflections exhibit a hyperbolic shape, such as for PcP, ScS, PcS and ScP. The phases PcS and ScP coincide with each other when the source is located at the Earth surface (Fig. 10a) and separate from each other with increasing focal depth (Figs 10b–d).

For ease of comparison, the receiver locations are the same as in the AK135 traveltime tables, that is, at an interval of 2°. Tables 1–4 give the maximum absolute traveltime errors (E1), the average absolute traveltime errors (E2), the maximum relative traveltime errors (E3) and the average relative traveltime errors (E4) against the AK135 traveltime tables for these 49 global phases. From the
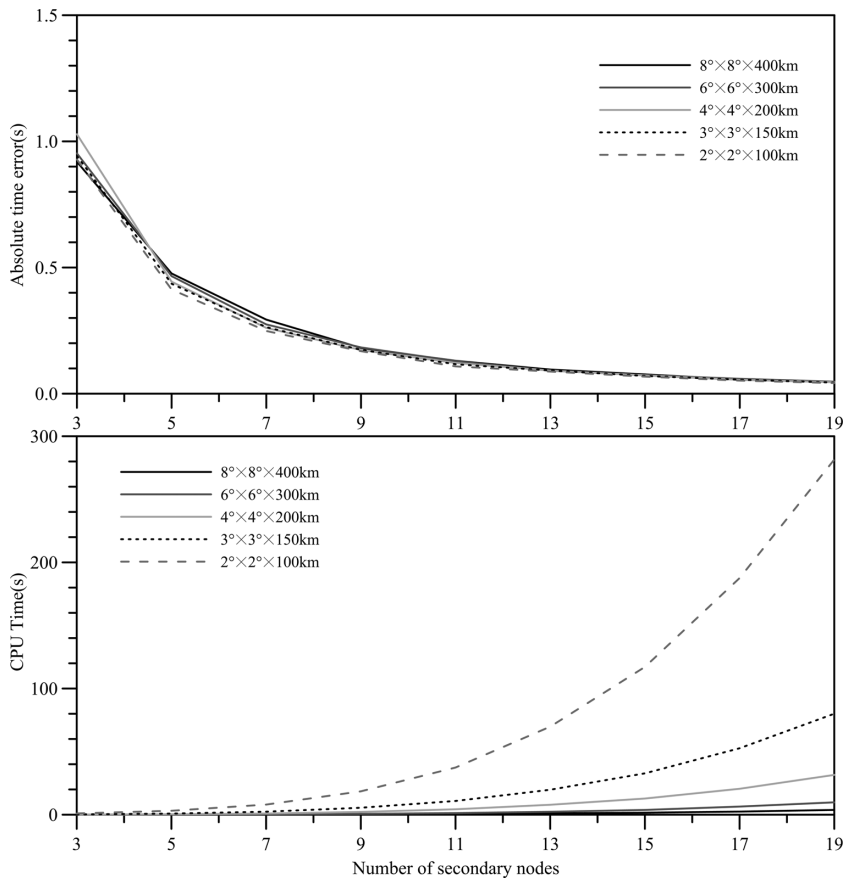
Figure 12. Tests for computational accuracy and efficiency for 3-D regional model with changing cell size and number of secondary nodes (diagram a: accuracy test; diagram b: computational efficiency and diagram c: the total number of the nodes via the number of added secondary nodes).

tables we may draw the following conclusions: (1) for almost all the phases the maximum absolute traveltime error is less than 0.12 s, and the average absolute traveltime is within 0.09 s (except for phase PKPab); (2) the computed *S*-mode phases have slightly larger absolute traveltime errors than those of the *P*-mode phases; (3) the computed traveltime errors against the reference AK135 tables have similar error features, regardless of source focal depth and (4) for global traveltimes it is meaningless to cite the relative traveltime errors. Taking the phase PKPab as an example, the maximum absolute time error is over 1.6 s but the maximum relative time error is only about 0.13 per cent, due to the long time associated with its long propagation path.

To appreciate the variations of traveltime error patterns with changes of epicentral distance, we show in Fig. 11 the time differences (or time errors) between the calculated and the AK135 traveltimes as a function of epicentral distance (diagram a: for focal depth of 0.0 km; diagram b: for focal depth of 100.0 km; diagram c: for focal depth of 300.0 km and diagram c: for focal depth of 600.0 km). From Fig. 11 it is obvious that the error curves are fluctuated slightly above zero value (within 0.1 s). Basically, the traveltime errors of the *S*-mode waves are larger than those of the *P*-mode waves, which increase slightly with epicentral distance, due to relatively longer time taken. Meanwhile, the error patterns are independent of the focal depth. The largest errors (see Tables 1–4 and Figs 11a–d) occur in the prediction of the PKPab phase, due to a couple of source–receiver pairs missing the outer core paths (see Fig. 9).

In summary, the multistage ISPM is capable of predicting most global main phases with a high computational accuracy, less than 0.1 s absolute traveltime errors compared with the AK135 theoretical traveltime tables. Such computational accuracy is high enough to enable regional or global traveltime tomographic studies.

5 COMPUTATIONAL EFFICIENCY

For the multistage ISPM in 2-D polar coordinates (see Fig. 1a), there is no problem with CPU time consumption, but for the multistage ISPM in 3-D spherical coordinates, the CPU time has to be taken into consideration. 3-D global or regional traveltime tomography usually requires millions of multiphase arrivals to be predicted and the forward modelling needs to be repeated several or dozens of times in the inversion model updating process. Therefore, a really fast and accurate 3-D ray tracing scheme is highly beneficial. For these reasons, it is useful to estimate the CPU time in 3-D applications.

We select a uniform spherical regional earth model (8.0 km s^{-1}) to estimate the computational accuracy and especially the CPU time to calculate the first *P* arrivals. The scale of the velocity model is 24° × 24° × 1200 km and there are five kinds of the trapezoidal prism cells (i.e. 8° × 8° × 400 km, 6° × 6° × 300 km, 4° × 4° × 200 km, 3° × 3° × 150 km and 2° × 2° × 100 km) to parametrize the velocity model. There are 625 receivers located uniformly over the model surface (i.e. 1° × 1° spacing) and the source is located at the co-ordinate origin at a depth of 100 km. To evaluate the influences of secondary node spacing in terms of computational efficiency and CPU time consumption, the added secondary node number increases from 3 to 19 for those five kinds of differently parametrized velocity models. The computer used here is a 2.8 GHz Intel Core i5-2300 with 4 GB memory. Fig. 12 shows the mean absolute traveltime errors (diagram a), the CPU time (diagram b) and the total number of nodes (diagram c) for the five different kinds of parametrized velocity models, as a function of secondary node

number (strictly speaking, it is the secondary node spacing, which equals the length of the cell divided by the number of secondary nodes). From Fig. 12(a) we see that the computed traveltime errors are independent of the selected trapezoidal prism cells, but depend on the number of added secondary nodes. With 7, 9 and 13 secondary nodes, the mean absolute time error is less than 0.3, 0.2 and 0.1 s, respectively. The CPU time consumption and also the total number of nodes are highly dependent on both the selected cell size for the model parametrization and the number of added secondary nodes for accuracy improvement. It increases according to the power law $n^2 \ln_2 n$, where n is the number of added secondary nodes (see Bai *et al.* 2007). Such conclusions are similar to previous results when the MSPM or ISPM schemes are applied in 2-D/3-D Cartesian coordinates (Bai *et al.* 2007, 2009, 2010). In real applications we should select a suitable cell size to divide the target velocity model


(a)

(b)
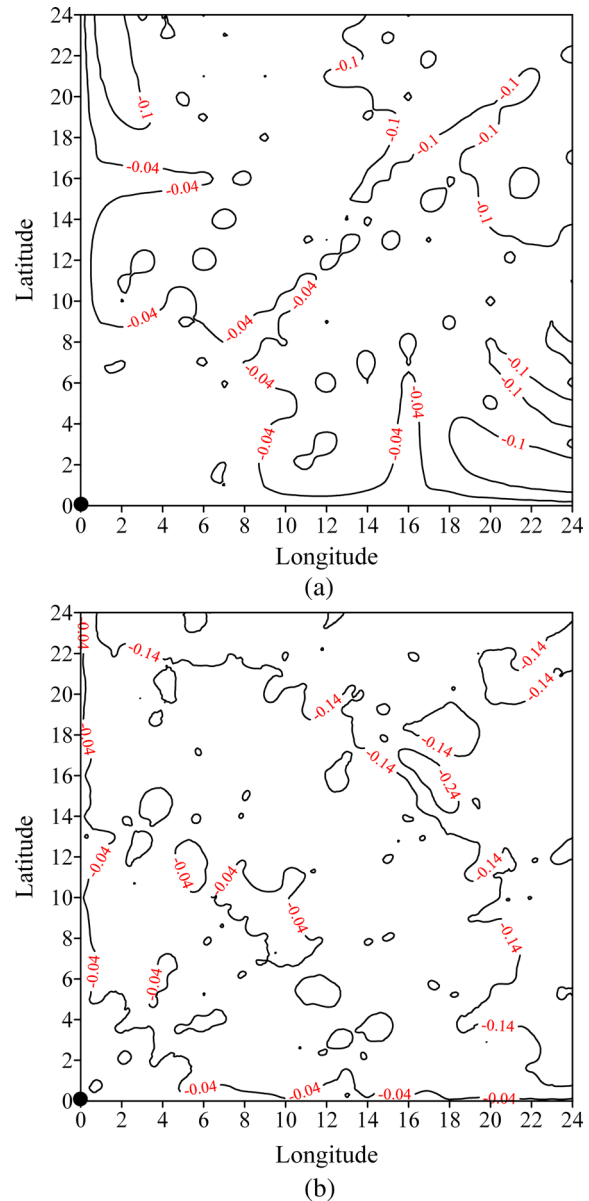
Figure 13. Contour plots of the direct *P*-wave arrival time errors on the surface for two models (diagram a: uniform velocity model and diagram b: AK135 velocity model). The source is located at 100 km depth under the model origin and 0.5° × 0.5° receiver spacing applied on the model surface. In the figure the solid black circle indicates the epicentre.

(according to the velocity field variation) and add enough secondary nodes to achieve the required computational accuracy. For example, to obtain a 0.2 s computational accuracy (absolute traveltime error) when the smallest cell size ($2° \times 2° \times 100$ km) is used and nine secondary nodes applied, the CPU time consumption is less than 20 s for that computed velocity model (see Fig. 12b). Such accuracy and CPU time are easy to achieve and the new method therefore is highly recommended for regional or global traveltime tomographic studies.

To inspect the error distribution on the Earth's surface, here we select two velocity models: one is the uniform velocity model of 8.0 km s^{-1} as used above and the other is the AK135 velocity model. The model scale and source–receiver layout are the same as described above. The cell size we selected is $2° \times 2°$ and secondary node spacing is 5 km. The traveltimes of the direct P wave were calculated and the error distributions on the Earth's surface are shown in Fig. 13 (diagram a: for uniform velocity model and diagram b: for AK135 velocity model). From Fig. 13 both error patterns are symmetric with respect to the source location, and the traveltime errors are increase slightly with increasing epicentral distance. For the uniform velocity model the largest error is less than 0.14 s (Fig. 13a) and for the AK135 model it is less than 0.24 s (Fig. 13b). Note that such errors can be further reduced by decreasing the secondary node spacing.

6 3-D MULTIPLE RAY PATHS

To visualize the performance of 3-D multiphase ray tracing, we select a regional scale layered velocity model (model scale is $15° \times 15° \times 700$ km, see Fig. 14), in which the velocity field changes both with longitude φ and depth. In the longitude direction the velocity field varies according to a $\sin(\varphi)$ function with a ±0.25 km s^{-1} fluctuation. In depth, the velocity increases linearly from the top surface at 5.0 km s^{-1} to the model base where the velocity is of 10.9 km s^{-1}. There are two undulating subsurface interfaces located at depths of 410 and 660 km, respectively. For model parametrization, a trapezoidal prism cell of size $1° \times ° 50$ km is used and the secondary node spacing is 2.0 km. The source is located at the model centre line at 100 km depth, and 46 receivers are located at the three edges (not the front edge) of the model surface at $1°$ uniform spacing. Fig. 13(a) shows the ray paths of the direct P arrivals and the primary reflections both from the 410 km discontinuity (phase P410P) and the 660 km discontinuity (phase P660P). Fig. 13(b) shows the ray paths of the double (two times) reflections between the Earth's surface and the 410 discontinuity (phase pP410P), and between the Earth's surface and the 660 km discontinuity (phase pP660P). More complicated multiphase arrivals can be predicted in this way.
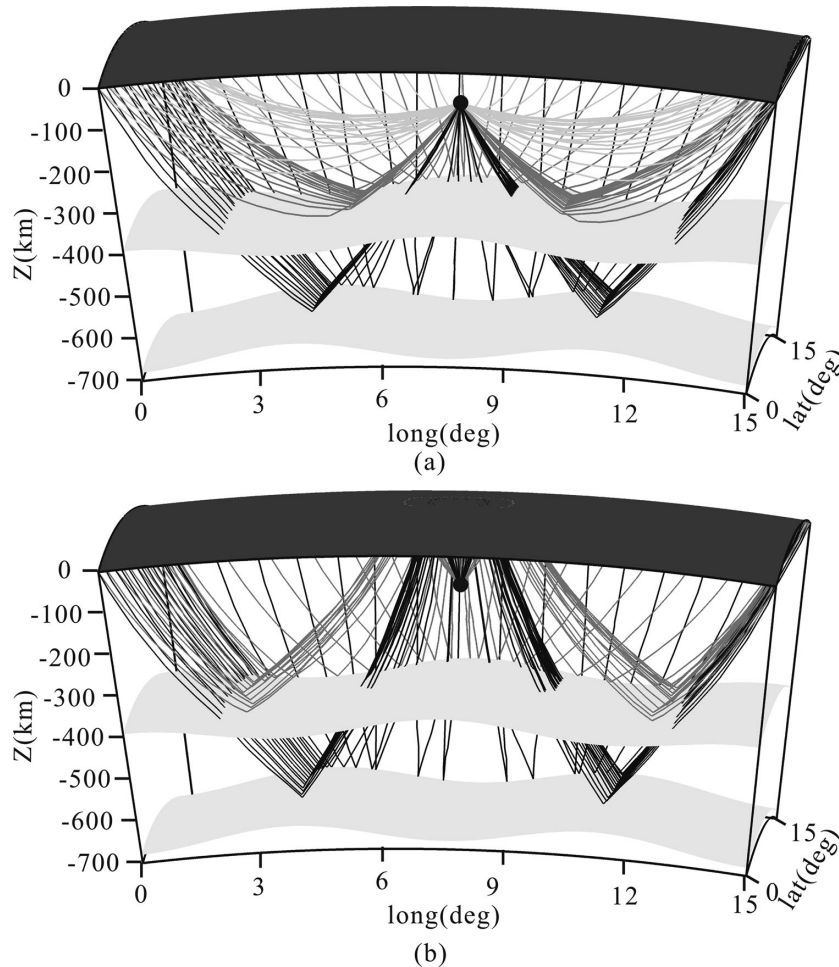
Figure 14. Multiple ray paths in a realistic 3-D regional velocity model. Diagram a: for direct P (grey lines), and reflections both from the 410 km discontinuity (P410P, dark grey lines) and the 660 km discontinuity (P660P, black lines) and diagram b: two-time reflections between the Earth's surface and the 410 km discontinuity (pP410P, grey lines) and between the Earth's surface and the 660 km discontinuity (pP660P, black lines).

7 DISCUSSION AND CONCLUSIONS

To calculate the later arrivals having stationary ray paths, we introduce the concept of Fermat's Principle of stationary minimax time paths, and extend the functional of the multistage ISPM scheme (Bai *et al.* 2010), previously only developed for Cartesian coordinates. This allows us to compute ray paths and traveltimes in spherical coordinates for 2-D/3-D velocity models to trace multiple later arriving of global phases for the Earth. The computational accuracy for the 49 predicted main global phases (except for the PKPab phase) is very good, with absolute errors of less than 0.09 s when compared with the AK135 theoretical traveltime tables (Kennett *et al.* 1995). The new formulation can be used to generalize regional or global traveltime tables for use in earthquake location. Furthermore, the scheme is computationally efficient with CPU time small enough for regional and global traveltime tomographic studies, for example, the CPU time on a standard PC is less than 1 min to calculate the response for a model involving millions of nodes with a suitable trapezoidal prism cell to divide the velocity structure (see Fig. 11). The method can be very suitable for tomographic purposes to delineate crust, mantle, even whole Earth velocity structure and velocity discontinuities with multiple classes of arrivals. In summary, the multistage ISPM performs as well in spherical coordinates as previously shown in Cartesian coordinates, in terms of both computational accuracy and CPU time.

ACKNOWLEDGEMENTS

REFERENCES

Aki, K. & Lee, W.H.K., 1976. Determination of three dimensional velocity anomalies under a seismic array using first P arrival times from local earthquakes, *J. geophys. Res.,* **81,** 4381–4399.

Anderson, D.L. & Dziewonski, A.M., 1982. Upper mantle anisotropy: evidence from free oscillations, *Geophys. J. R. astr. Soc.,* **69,** 383–404.

Bai, C.Y., Greenhalgh, S. & Zhou, B., 2007. 3D ray tracing with a modified shortest path method, *Geophysics,* **72,** T27–T36.

Bai, C.Y., Tang, X.P. & Zhao, R., 2009. 2D/3D multiply transmitted, converted and reflected arrivals in complex layered media with the modified shortest path method, *Geophys. J. Int.,* **179,** 201–214.

Bai, C.Y., Huang, G.J. & Zhao, R., 2010. 2D/3D irregular shortest-path raytracing for multiple arrivals and its applications, *Geophys. J. Int.,* **183,** 1593–1612.

Bai, C.Y., Li, X.L. & Tang, X.P., 2011. Seismic wavefront evolution of multiply reflected, transmitted and converted phases in 2D/3D triangular cell model, *J. Seismol.,* **15,** 637–652.

Bai, C.Y., Li, X.L., Wang, Q.L. & Peng, J.B., 2012a. Multiple arrival tracking within irregular triangular or tetrahedron cell model, *J. geophys. Eng.,* **9,** 29–38.

Bai, C.Y., Huang, G.J., Tang, X.P. & Greenhalgh, S., 2012b. Multi-valued reflection arrival tracking via an extremal solution of the summed ray field, *J. geophys. Eng.,* **9,** 549–557.

Ballard, S., Hipp, J.R. & Yang, C.J., 2009. Efficient and accurate calculation of ray theory seismic travel time through variable resolution 3D earth models, *Seism. Res. Lett.,* **80,** 989–999.

Bormann, P., Engdahl, B. & Kind, R., 2009. Seismic wave propagation and earth models, in *New Manual of Seismological Observatory Practice (NMSOP),* pp. 1–70, ed. Bormann, P., Potsdam: Deutsches Geo-Forschungs Zentrum GFZ.

Bijwaard, H. & Spakman, W., 1999. Fast kinematic ray tracing of first- and later-arriving global seismic phase, *Geophys. J. Int.,* **139,** 359–369.

Bijwaard, H. & Spakman, W., 2000. Non-linear global P-wave tomography by iterated linearized inversion, *Geophys. J. Int.,* **141,** 71–82.

Cerveny, V., 2001. *Seismic Ray Theory,* Cambridge University Press, Cambridge, UK.

Dahlen, F.A., Hung, S.-H. & Nolet, G., 2000. Fréchet kernels for ffinite-frequency traveltimes – I, Theory, *Geophys. J. Int.,* **141,** 157–174.

De Kool, M., Rawlinson, N. & Sambridge, M., 2006. A practical grid-based method for tracking multiple refraction and reflection phases in three-dimensional heterogeneous media, *Geophys. J. Int.,* **167,** 253–270.

Dziewonski, A.M. & Gilbert, F., 1976. The effect of small, aspherical perturbations on travel times and a re-examination of the corrections for ellipticity, *Geophys. J. R. astr. Soc.,* **44,** 7–17.

Dziewonski, A.M. & Anderson, D.L., 1981. Preliminary reference earth model, *Phys. Earth planet. Inter.,* **25,** 297–356.

Kennett, B.L.N. & Engdahl, E.R., 1991. Traveltimes for global earthquake location and phase identification, *Geophys. J. Int.,* **122,** 429–465.

Kennett, B.L.N., Engdahl, E.R. & Buland, R., 1995. Constraints on seismic velocities in the earth from traveltimes, *Geophys. J. Int.,* **122,** 108–124.

Keyser, J.R., Ritter, R. & Jordan, M., 2002. 3D shear-wave velocity structure of the Eifel plume, Germany, *Earth planet. Sci. Lett.,* **203,** 59–82.

Klimeš, L. & Kvasnička, M., 1994. 3-D network ray tracing, *Geophys. J. Int.,* **116,** 726–738.

Moser, T.J., 1991. Shortest path calculation of seismic rays, *Geophysics,* **56,** 59–67.

Pratt, R.G. & Chapman, C.H., 1992. Travel Time tomography in anisotropic media: II. Application, *Geophys. J. Int.,* **109,** 20–37.

Rawlinson, N. & Sambridge, M., 2004a. Wavefront evolution in strongly heterogeneous layered media using the fast marching method, *Geophys. J. Int.,* **156,** 631–647.

Rawlinson, N. & Sambridge, M., 2004b. Multiple reflection and transmission phases in complex layered media using a multistage fast marching method, *Geophysics,* **69,** 1338–1350.

Snoke, J.A. & Lahr, J.C., 2001. Locating earthquakes: at what distance can the earth no longer be treated as flat? *Seism. Res. Lett.,* **72,** 538–541.

Steck, L.K., Thurber, C.H., Fehler, M.C., Lutter, W.J., Roberts, P.M., Baldridge, W.S., Stafford, D.G. & Sessions, R., 1998. Crust and upper mantle P wave velocity structure beneath Valles caldera, New Mexico: results from the Jemez teleseismic tomography experiment, *J. geophys. Res.,* **103,** 24 301–24 320.

Storchak, D.A., Schweitzer, J. & Bormann, P., 2003. The IASPEI standard seismic phase list, *Seism. Res. Lett.,* **74,** 761–772.

Su, W.J., Woodward, R.L. & Dziewonski, A.M., 1994. Degree-12 model of shear velocity heterogeneity in the mantle, *J. geophys. Res.,* **99,** 6945–6980.

Thomsen, L., 1986. Weak elastic anisotropy, *Geophysics,* **51,** 1954–1966.

van der Hilst, R.D., Widiyantoro, S. & Engdahl, E.R., 1997. Evidence for deep mantle circulation from global tomography, *Nature,* **386,** 578–584.

Vidale, J.E., 1988. Finite-difference calculation of travel times, *Bull. seism. Soc. Am.,* **78,** 2062–2076.

Vidale, J.E., 1990. Finite-difference calculation of travel time in three dimensions, *Geophysics,* **55,** 521–526.

Zhao, D., Hasegawa, A. & Horiuchi, S., 1992. Tomographic imaging of P and s wave velocity structure beneath northeastern Japan, *J. geophys. Res.,* **97,** 19 909–19 928.

Zhao, D., 2001. Seismic structure and origin of hotspots and mantle plumes, *Earth planet. Sci. Lett.,* **192,** 251–265.

Zhao, D.P. & Lei, J.S., 2004. Seismic ray path variations in a 3D global velocity model, *Phys. Earth planet. Inter.,* **141,** 153–166.